Acoustic Fault Detection Technique for High-Power Insulators

Kyu-Chil Park, Yuichi Motai, *Senior Member, IEEE*, and Jong Rak Yoon

***Abstract*—Insulators are important equipment used to electrically isolate and mechanically hold wires in high-voltage power transmission systems. Faults caused by the deterioration of the insulators induce very serious problems to the power transmission line. Techniques were introduced for the acoustic detection of insulator faults by acoustic radiation noises. Radiation noises were measured from normal state insulators and fault state insulators in an anechoic chamber. The insulators used were two porcelain insulators, a cut-out switch, two line posters, and a lightning arrester. A new acoustic technique determines the direction of the insulator faults using source localization with three-dimensional microphone arrays. The advantage is to classify the fault state insulators without human inspection by considering the amount of total noises and 120-Hz harmonic components. The fault detection was determined by neural network to diagnose the state automatically. The proposed technique was evaluated by distinct, real datasets and the efficacy was validated. The noise source was detected with 100.0% accuracy and the classification ratio achieved 96.7% for three typical conditions.**

***Index Terms*—Insulator, neural network (NN), peak detection, radiation noise, source localization.**

I. INTRODUCTION

INSULATORS are used for the mechanical holding of the wires and the electrical insulating in the transmission line system. Since the failure of such insulators causes a large barrier to having a high-quality power supply, the detection of insulator faults is necessary for improving the stability and reliability of the power system for replacement or diagnosis [1]–[5]. The insulator failures are mainly classified problems caused by microscopic defects or cracks in the manufacturing process or by deterioration due to lightning, cold, or salinity after installation on power plants. The problem of the manufacturing process is detected upon sufficient inspection before the installation, but the problem of the deterioration after the installation requires periodic diagnosis.

Looking at the breakdown process simply, it is known that the insulator is aging, or damaged so that feeble discharge occurs, then electrical destruction of the oxide ensures, and finally the isolation of insulators is destroyed. As the thickness of the insulator's oxide film is between 0.001 and 0.01 in, a breakdown process is defined as a microspark, not arc or spark. It is known that the breakdown occurs when the voltage is larger than the threshold voltage of the oxide film's breakdown voltage [1]–[3]. The methods for detecting a faulty isolation insulator with deterioration use voltage division and the insulation resistance, the electric field, ultrasonic waves, an infrared/ultraviolet sensor camera, and so on [2], [3]. Each method has advantages and disadvantages in the reliability of the detection results, detecting times, price, or stability. Since an insulator suffers from various issues, it is difficult to determine the best measurement method to cover the varieties of all the faults. The advantage is to classify the fault state insulators without human inspection.

There is a noise source detection system using a microphone array in [2]. As it has three microphones to estimate the three-dimensional (3-D) position of the fault insulator, it measures the noises twice at two different measurement positions, and reconstructs six microphones' data processing to represent the noise source position. Since our system has four microphone array in 3-D structure, it is possible to estimate the noise position with just one time measurement.

This paper demonstrates the effective capability of the combination of acoustic source detection and fault detection. The demanding problem of how to automatically determine the status of a power insulator is solved by developing an acoustic sensor system. A sound detection system mounted to a robot operating on the top of the pole wires, using measurement and analysis of the radiated noise from the insulator, was developed. Six insulators were measured and analyzed—two porcelain insulators (PIs), a cut-out switch (COS), two line posters (LPs), and a lightning arrester. For comparison, the radiated noise was measured from a normal state insulator and a fault state insulator, then the frequency spectrum characteristics were analyzed so that it could be determined whether the insulator faulted.

This paper is organized as follows. In Section II, the relevant studies are listed. In Section III, the proposed insulator noise detection techniques are presented in detail. Section IV presents and discusses experimental results of proposed methods. A summary of the performance of the proposed method is presented in Section V.

Manuscript received November 30, 2016; revised April 4, 2017, April 27, 2017, and May 8, 2017; accepted May 17, 2017. Date of publication June 16, 2017; date of current version October 24, 2017. This work was supported in part by the Pukyong National University Research Abroad Fund in 2015 (C-D-2015-0514), and in part by the National Science Foundation under Grant 1054333. *(Corresponding author: Yuichi Motai.)*

K.-C. Park and J. R. Yoon are with the Department of Information and Communications Engineering, Pukyong National University, Busan 48513, South Korea (e-mail: kcpark@pknu.ac.kr; jryoon@pknu.ac.kr).

Y. Motai is with the Electrical Engineering Department, Virginia Commonwealth University, Richmond, VA 23284 USA (e-mail: ymotai@vcu.edu).

Color versions of one or more of the figures in this paper are available online at http://ieeexplore.ieee.org.

Digital Object Identifier 10.1109/TIE.2017.2716862

TABLE I
REPRESENTATIVE STUDIES ON FAULT DIAGNOSIS SYSTEMS

Category	Representative studies and characteristics
Transient [6]	Optimize the transient response of proportional-resonant current controllers.
Imbalance [7]	Stationary-frame control for voltage unbalance compensation in an islanded microgrid.
Waveform distortion [8]–[10]	Adaptive linear network for harmonic and interharmonic estimation. Reduce the tracking error and compensate harmonics of the inverter systems. Selective harmonic detection system.
Fault monitoring [11]–[13]	Adaptive multiscale noise for a health diagnosis under stochastic resoinance conditions. Phase control scheme based on diagnosis of energy conversion system. Real-time algorithm to monitor electric motors.

II. RELEVANT STUDIES

The relevant studies are listed as fault diagnosis in Section II-A, noise source from the power line system in Section II-B, and array signal processing in Section II-C.

A. Fault Diagnosis

The monitoring of delivering electric power is affected by all equipment used for each specific domain. Fault diagnosis is evaluated by a set of electrical boundaries that allows a piece of equipment to function in its intended manner without significant loss of performance or life expectancy [4]. IEEE 1159 defines the power quality as the significant factor in [5].

Table I lists the representative studies on variations of power quality that may be used for fault diagnosis. To provide categories and typical characteristics of power system electromagnetic phenomena, power quality is affected by significant phenomena such as transients [6], imbalance [7], and waveform distortion [8]–[10]. The adaptive multiscale noise for a health diagnosis is developed [11], and real-time monitoring for electric motors can detect fault signatures effectively [12], [13].

B. Noise Source From the Power Line System

The noise source of the power line system is very diverse, but can be divided into main noise sources and minor noise sources [1], [2]. Table II shows the main noise sources. These radiated noises from the noise sources are generated by one independent noise source or in combination with other noise sources. The installation of the hardware components used for power companies is different, and the characteristics of the noise sources may vary from concrete/wood poles, and coated /noncoated wire ties. The noise sources of the power line system are complex, and consequently, they may be independent/dependent. Knowledge of the entire power line system is required to take appropriate measures in detecting them.

TABLE II
MAIN NOISE SOURCE OVER WIRE SYSTEM [1]

Rating	Source hardware
1	Bell insulator
2	Loose hardware
2	Lightning arrester
3	Insulated tie wires or bare tie wires on insulated conductors
3	Small discharges between inadequately spaced and unbonded metal components
3	Improperly assembled transitions between overhead conductors and underground lines

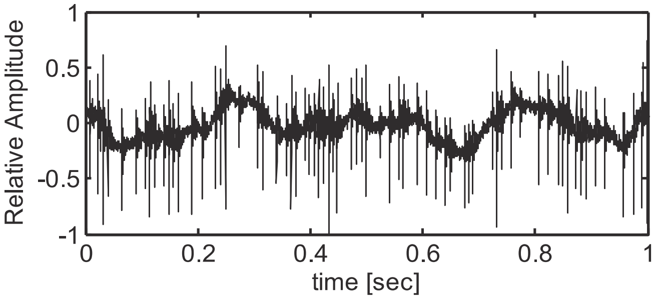

Fig. 1. Fault state insulator's time signal measured. It contains lots of spike signals. The period of the impulse groups is 8.3 or 16.6 ms according to the frequency of the electric voltage.

The bell insulator is one of the main targets of this study. Its average lifetime is 40 years. However, as it is a major source of noise, it becomes replaced by any other type of insulator. The noise of the bell insulator is related to the electrical breakdown of the oxide film on the surface of the insulator. The complicated fracture process is well identified on the basis of the circuit.

The thickness of the oxide film of the insulator is from 0.001 to 0.01 in, so the destructive process is not considered to be an arc or spark. It is defined as microsparks when the threshold voltage is larger than the breakdown voltage of the oxide film. It may be intensified by the addition of radio signals, lightning, and other transient voltage switching on the normal transmission voltage.Fig. 1 shows a time signal in a fault state of an insulator. If it takes place on the maximum or minimum value of the transmission voltage, impulse groups may be generated at a period of 16.6 ms.

It can be concluded that noise due to the noise source of the power line system represents a form of impulse like the microspark. Also, the period of the impulse groups is 8.3 or 16.6 ms according to the frequency of the electric voltage.

C. Array Signal Processing

The array signal processing techniques are used to identify the acoustic characterization or estimate the position of the noise source by the receiving signals with sensor arrays in space [14]. It has been widely adopted on military sonar, medical ultrasound diagnostic equipment, and vehicle noise detection equipment. The array processing techniques [15] on these devices are adopted from the beamforming method [16], MUSIC method [17], correlation function method [18], bispectrum method [19], sound intensity method [20], acoustic holography method [21], and so on. They are each determined if the

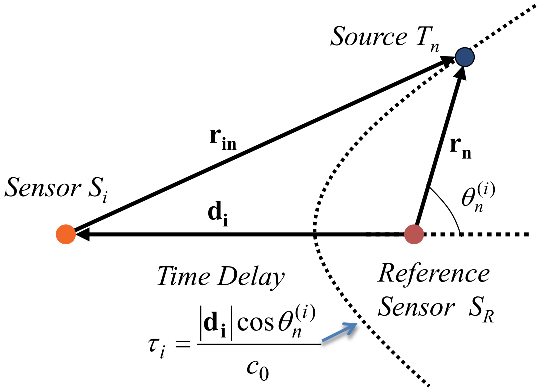

Fig. 2. Pair of sensors, sound source, and path length difference. The relative time delay can be estimated in a 2-D sensor system. The dots show the same time delay between two sensors.

application is in accordance with sound environment and purpose. The beamforming method and MUSIC method cannot be adopted because of the long distance detection on the target with narrow-band signal. The spatial measuring range of the sound intensity method and acoustic holography method is wide so that the robot's geometric size becomes large. It cannot be attached to a robot, and required a long computation time in long-term measured data. In this study, a correlation function method employs a technique to estimate the position of the fault insulators.

III. INSULATOR NOISE DETECTION

The proposed insulator noise detection consists of the following four modules. Cross-correlation function analysis of the array sensor received signal in Section III-A, noise source location estimation and arrangement in Section III-B, angular resolution and the grid size of the image plane in Section III-C, and the feature extraction techniques and neural network (NN) in Section III-D.

A. Cross-Correlation Function Analysis of the Array Sensor Received Signal

Considering two receivers as shown in Fig. 2, they assumed abnormal noises from insulators as uncorrelated broadband noise sources. Assuming that the reference sensor is at the coordinate origin, each position and volume velocity are defined as $\mathbf{r}_n$ and $Q_n(t)\ (n = 1, 2, \ldots, N)$, respectively. The measured sound pressures on the reference sensor and the arbitrary ith sensor is given by

$$P_0(t) = \sum_{n=1}^{N} \frac{\rho Q_n\left(t - \frac{|\mathbf{r}_n|}{c_0}\right)}{4\pi|\mathbf{r}_n|},\ P_i(t) = \sum_{n=1}^{N} \frac{\rho Q_n\left(t - \frac{|\mathbf{r}_{in}|}{c_0}\right)}{4\pi|\mathbf{r}_{in}|} \tag{1}$$

where $\mathbf{r}_{in} = \mathbf{r}_n - \mathbf{d}_i$ and the bold lower case denotes the vector. N, ρ, c_0, and $|\bullet|$ are the number of the noise sources, the density of air, the sound speed on air, and the norm, respectively.

From (1), the cross-correlation function $R_i(\tau)$ is given by [18]

$$\begin{aligned} R_i(\tau) &= \int_{-\infty}^{\infty} P_0(t)\,P_i(t+\tau)\,dt \\ &= \int_{-\infty}^{\infty} \sum_{n=1}^{N}\sum_{m=1}^{N} \frac{\rho^2 Q_n\left(t - \frac{|\mathbf{r}_n|}{c_0}\right) Q_m\left(t - \frac{|\mathbf{r}_{im}|}{c_0} + \tau\right)}{16\pi^2 |\mathbf{r}_n|\,|\mathbf{r}_{im}|}\,dt. \end{aligned} \tag{2}$$

Defining $D_{nm}(\tau)$ for the cross-correlation function between the nth and mth noise source, we obtain

$$D_{nm}(\tau) = \int_{-\infty}^{\infty} \rho^2 Q_n(t)\,Q_m(t+\tau)\,dt. \tag{3}$$

Since each source of noise is uncorrelated

$$D_{nm}(\tau) = \begin{cases} D_n(\tau) \neq 0, & \text{if } n = m, \\ 0, & \text{if } n \neq m. \end{cases} \tag{4}$$

Equation (2) by (3) and (4) is converted into the following equation:

$$\begin{aligned} R_i(\tau) &= \sum_{n=1}^{N} \frac{D_n\left(\tau - \frac{|\mathbf{r}_{in}| - |\mathbf{r}_n|}{c_0}\right)}{16\pi^2 |\mathbf{r}_n|\,|\mathbf{r}_{in}|} \\ &= \sum_{n=1}^{N} A_n D_n\left(\tau - \frac{|\mathbf{d}_i|\cos\left(\theta_n^{(i)}\right)}{c_0}\right) \end{aligned} \tag{5}$$

where $A_n = 1/(16\pi^2|\mathbf{r}_n||\mathbf{r}_{in}|)$. $\theta_n^{(i)}\ (n = 1, 2, \ldots, M)$ is the angular position forming between a straight line on the receivers and the nth noise source, as shown in Fig. 2. Therefore, the cross-correlation function of (5) will have a maximum value if the time delay function $\tau_n^{(i)}$ of each noise source satisfies the following conditions:

$$\tau_n^{(i)} = \frac{|\mathbf{d}_i|\cos\left(\theta_n^{(i)}\right)}{c_0}. \tag{6}$$

So, $\theta_n^{(i)}$ will be obtained from $\tau_n^{(i)}$ maximizing the cross-correlation function. If the noise source's characteristic is white noise, $R_i(\tau)$ will be the Dirac-delta function. However, the noise source's characteristic is a broadband signal, and it needs a prewhitening method. The radiated noise from the fault state insulator contained many spark signals with a 16-ms period, as shown in Fig. 1. It can be regarded that the signal is stationary on the length over 16 ms. In the present study, the smoothed coherence transform method [22] was adopted for the prewhitening method [23] to minimize the effects of external noise, given by

$$\begin{aligned} R_{x_1x_2}(\tau) &= F^{-1}\left[\frac{X_1X_2^*}{\sqrt{X_1X_1^* \bullet X_2X_2^*}}\right] = F^{-1}\left[e^{-j\omega\tau_1}\right] \\ &= \delta(\tau - \tau_1) \end{aligned} \tag{7}$$

where x_1 and x_2 are the received signals, X_1 and X_2 are their respective Fourier transforms, F^{-1} is the inverse Fourier transform, and $\delta(\bullet)$ is the Dirac-delta function. Cross-correlation

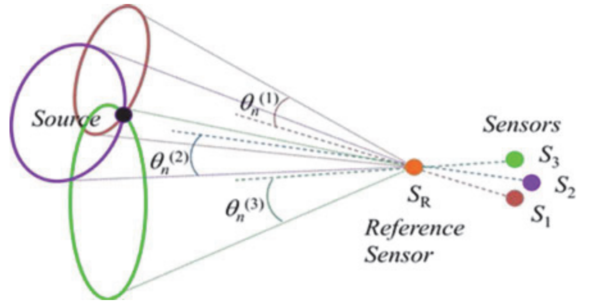

Fig. 3. Intersection of the conical surfaces. n is the angular position forming between a straight line on the sensors and nth noise source and it will be obtained by the cross-correlation function.

function analysis of the array sensor's result will be given by a delayed delta signal.

B. Noise Source Location Estimation and Arrangement

For the noise source location estimation, a 3-D array arrangement with four microphones was adopted. By applying (5) to the cross-correlation function between the reference sensor and the arbitrary ith sensor, the time delay index $\tau_n^{(i)}$ from (6) is given by

$$\tau_n^{(i)} = \frac{|d_i|\cos\left(\theta_n^{(i)}\right)}{c_0} \tag{8}$$

where $\theta_n^{(i)}$ the nth noise source is located in a circular arc, as shown in Fig. 3. It cannot be determined by only one array pair. Thus, at least three pairs of noise sources must be arranged in different planes in the space, so that the source position can be uniquely determined.

Let the number of array elements be K $(i = 1, 2, \ldots, K)$ and the number of the lattice points of the image plane corresponding to the noise source azimuth be $M \times N$. Each grid point is given by Z_{sp} $(s = 1, 2, \ldots, M;\ p = 1, 2, \ldots, N)$, where the focal length is defined as the distance between the image plane and the reference point, as shown in Fig. 4. Therefore, the time delay index $\tau_{sp}^{(i)}$ between each image point of the image plane Z_{sp} and the ith sensor pairs is given by

$$\tau_{sp}^{(i)} = \frac{|Z_{sp} - d_i| - |Z_{sp}|}{c_0}. \tag{9}$$

As the nth sound source is located on the image of the source r_n, the image of the projected source to the image plane is defined as shown in Fig. 4. Therefore, the image point of the source is given by

$$|z_{sp} - d_i| - |z_{sp}| = |r_n - d_i| - |r_n| = \tau_{sp}^{(i)} c_0. \tag{10}$$

When (10) is satisfied, the cross-correlation function $R_i(\tau_{sp}^{(i)})$ will have a maximum value. Therefore, the value of $R_i(\tau_{sp}^{(i)})$ put on the Z_{sp} allows an image corresponding to the orientation of the noise source to be obtained.

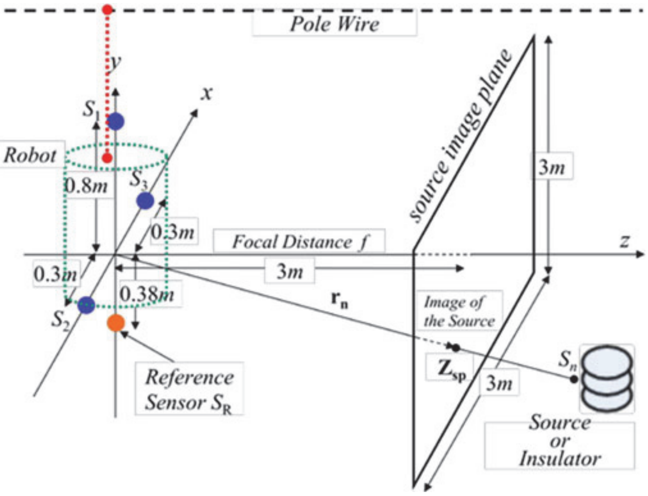

Fig. 4. Array geometry, coordinate, and source image plane. The sound source can be imaged in the source image plane with three sets of time delay, as shown in Fig. 3.

C. Angular Resolution and the Grid Size of the Image Plane

In order to separate two adjacent noise sources, the arrangement should be designed so that the maximum value of the correlation function can be imaged. It is also necessary for the geometrical interpretation of the geometric distance between the sensors, and the maximum resolution dependent on the band characteristics of the noise source.

It is assumed that there exist two adjacent noise sources K, L, and image point positions Z_k and Z_l. The time delay index for the ith sensor pair is given by the following equations, respectively,

$$\tau_k^{(i)} = \frac{|z_k - d_i| - |z_k|}{c_0}, \quad \tau_l^{(i)} = \frac{|z_l - d_i| - |z_l|}{c_0}. \tag{11}$$

Using (8) and (11), the difference $\Delta\tau^{(i)}$ in the time delay index for each noise source is given by

$$\Delta\tau^{(i)} = \tau_k^{(i)} - \tau_l^{(i)} = \frac{|d_i|}{c_0}\left(\cos\left(\theta_k^{(i)}\right) - \cos\left(\theta_l^{(i)}\right)\right). \tag{12}$$

In addition, let $\theta_k^{(i)} = \theta_l^{(i)} - \Delta\theta$, then (12) is approximated by the following equation:

$$\Delta\tau^{(i)} = \frac{|d_i|}{c_0}\sin\left(\theta_l^{(i)}\right). \tag{13}$$

When the bandwidth of the noise source is B, the minimum time difference $\Delta\tau_{\min}^{(i)}$ can be approximated by $1/2B$. It can seperate the time delay index corresponding to the maximum value on each noise source on the cross-correlation function. Therefore, $|\Delta\theta|$ is given by

$$|\Delta\theta| > \left(\frac{c_0}{2B\,|d_i|\sin\left(\theta_l^{(i)}\right)}\right) \tag{14}$$

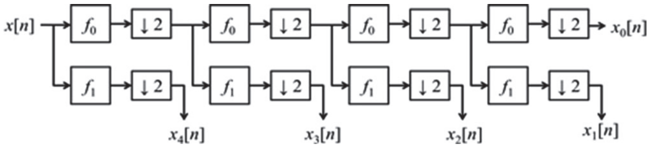

Fig. 5. Multiresolution filter bank. It divides a whole signal into five different width signals in the frequency domains like as 0 kHz ~ 1 kHz, 1 kHz ~ 2 kHz, 2 kHz ~ 4 kHz, 4 kHz ~ 8 kHz, and 8 kHz ~ 16 kHz. ↓ 2 means a factor-of-2 down sampler.

In addition, because the lattice point-to-point distance Δz of the image plane is relatively small compared to the focal distance f, $\theta \approx z/f$. Therefore, Δz in the image plane is given by

$$|\Delta z| > \frac{f c_0}{2B |d_i| \sin \theta_l^{(i)}} \tag{15}$$

The resolution and the image plane size of each grid point in the array is determined by the distance $|d_i|$ between the sensors, the sound source position $\theta_l^{(i)}$, the bandwidth B, and the focal distance f of the noise source.

D. Feature Extraction Techniques and NN

The radiated sound signal from the insulator has a nonuniform background, and it also contains peak components in a fault state owing to the microsparks. The amount of background noises and peak components are important factors to know the signal's power and peak components' level, respectively. However, the peak signal can be buried by a nonuniform background signal. So, both the sector space averaging technique and the filter bank analysis are applied.

In the sector space averaging technique [24], the following filter is used through the entire frequency spectrum:

$$y[n] = x[n] - \frac{1}{2N} \sum_{k=1}^{N} \{x[n-k] + x[n+k]\} \tag{16}$$

where N is the number for the filter length. The frequency response of (16) is the high-pass filter so that the microsparks will remain. It can also attenuate the slowly varying nonuniform noise background. $x[n]$ and $y[n]$ are the input and the output of the filter, respectively. Its frequency characteristic shows an ideal low-frequency reject filter.

The filter bank used to extract the divergence of the entire frequency spectrum is shown in Fig. 5. The signal is divided into several separate frequency domains such as 0 kHz ~ 1 kHz (FB1), 1 kHz ~ 2 kHz(FB2), 2 kHz ~ 4 kHz(FB3), 4 kHz ~ 8 kHz(FB4), and 8 kHz ~ 16 kHz(FB5). These five data domains are used for the input to the curve fitting function. The algorithm used is the curve fitting library of exponential models (a single-term exponential) in the MATLAB toolbox. Among the results, the exponent part will be used for the input parameters of the NN for the classification.

For the classification of the insulators' state, the pattern recognition technique with a NN, as shown in Fig. 6, will be applied.

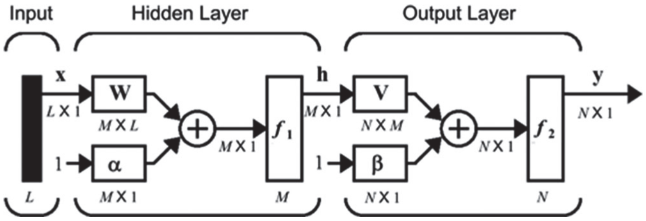

Fig. 6. Block diagram of a NN. It is a multilayer feed-forward networks with one-hidden layer fully connected network. *L*, *M*, and *N* are number of elements in input, hidden, and output layer, respectively [25].

It is a multilayer feed-forward network with one-hidden layer fully connected network. L, M, and N are a number of elements in the input, hidden, and output layers, respectively. The hidden layer has a weight matrix W, a bias vector α, a decision function f_1, and an output vector h. The output layer also has a weight matrix V, a bias vector β, a decision function f_2, and an output vector y. The outputs on each layer is given by

$$h = f_1(W x + \alpha), \quad y = f_2(V h + \beta). \tag{17}$$

The classification using NN is summarized in the pseudocode as follows:

```
Classification of the insulator using Neural Network
Input: x: input feature data
    1st data: an exponent part from fitting curve from
    filter bank results
    2nd-6th data: amplitudes of harmonic component of
    120 Hz
    7th data: an average from 60 Hz to 660 Hz
Learning/Training: define the weighting on the network
    Repeat following 3 steps to minimize the error
      1) output from the hidden layer
         for $m = 0$ to $M - 1$ do
            $h_m = f_1(W_{ml} x_l + \alpha_m)$
         end for
      2) output from the output layer
         for $n = 0$ to $N - 1$ do
            $y_n = f_2(\sum_m V_{nm} h_m + \beta_n)$
         end for
      3) minimize the cost function (sum squared error)
         $C = (y_k - y_l)^2$
Output: y: classification result given by normal or fault
      for $p = 0$ to $P - 1$ do
         [normal or fault] = max(logsig($y_p$))
      end for
P: the number of samples for classification.
```

The used transfer function of each layer was logsig (logarithmic sigmoid transfer function), the back-propagation network training function was traingd (gradient descent back propagation), and the cost function was sum squared error.

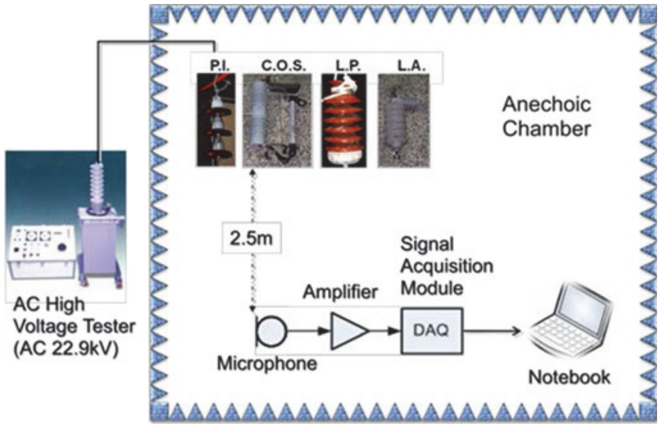

Fig. 7. Block diagram for measurement noises from the insulators. Both the normal state and the fault state of four types of the insulators were measured one by one with sampling frequency 40 kHz in the anechoic chamber [3]. The entire average SPL of ambient noise was 30.51 dB and the average SPL from first to fifth harmonics of 120 Hz was 45.33 dB.

IV. EXPERIMENTAL RESULTS

The ambient noise in the anechoic chamber was measured and evaluated for comparison with the insulators' noises in Section IV-A. The insulators' noises were also measured and evaluated in Section IV-B, the detection of the fault insulators' direction with the 3-D array system in Section IV-C, and the NN for the decision of the fault, or lack thereof, in Section IV-D.

A. Datasets

Insulators' noise measurement and analysis methods are developed. First, the background noise was measured in the anechoic chamber with the system, as shown in Fig. 7. As the acoustic detection system, which is mounted on the robot to operate at the top of the pole wires, was located less than 3 m from the source to the front end, it was measured with 2.5-m distance in the anechoic chamber. The measurement system consisted of four B&K 1/2 in condenser microphones Type 4130, four preamplifiers B&K Type 2642 with the power supply B&K Type 2810, and a data acquisition device NI USB-9233. As the received sound's frequency range of the microphone is 5 Hz–12.5 kHz on the response –3 dB, the sampling frequency was set to be 40 kHz. Both radiation noises of the normal state and the fault state insulator were measured one by one.

Two different analysis methods were attempted by analyzing the frequency characteristics of the measured time signals using Fourier transform with a channel 16 384 point data (achieved from microphone channel 2). The wideband (0–20 kHz) analysis is for looking up the characteristics of the entire frequency spectrum, evaluating its average level, the harmonics components of the 120 Hz, and the peak frequency detection for extracting the harmonic component in the narrow band (0–1 kHz). Table III shows the dataset to be measured. As the fault state's standard deviation is larger than the normal state's, the power of the fault state is also larger than the normal state. In the same way as ambient noise measurement and analysis, the normal state and the fault state of the four types of the insulators' noises were measured and evaluated in Section IV-B.

TABLE III
TYPES OF INSULATORS FOR MEASUREMENT

Type	Differences	Statistical property: Std (normal/fault)
PI	P.I.1: 2 plates	0.3186/0.6702
	P.I.2: 3 plates	0.2877/0.4351
COS		0.2583/0.3063
LP	L.P.1: company A	0.2565/0.3620
	L.P.2: company B	0.2524/0.3022
LA		0.2679/0.2771

Std: standard deviation.

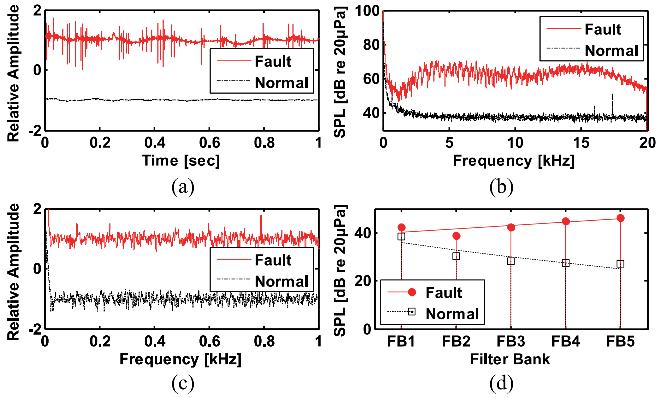

(a) (b) (c) (d)

Fig. 8. Comparison between the normal state and the fault state of the PI type 1 (P.I.1): (a) time signal, (b) frequency spectrum, (c) peak detection, and (d) filter bank and its fitting curve. The fault state had values 16.18 and 8.13 dB larger, than those of the normal state in the entire average SPL and the average SPL from first to fifth harmonics of 120 Hz, respectively. The exponent values of normal and fault were –0.09 and 0.03, respectively.

Before the measurement of the insulators' noises, the ambient noise was measured and evaluated. The results of the ambient noise's characteristics closely resembled Fig. 8(b)'s normal state insulator's ambient noise in the wideband analysis and peak detection. At the frequency spectrum in wideband analysis, it degraded exponentially under 3 kHz and had the flat characteristics over 3 kHz. There several unexpected peak components were found at approximately 800 Hz, 1.6 kHz, 12 kHz, 15 kHz, and 17 kHz. All measured data from insulators also showed a similar frequency characteristics, so these frequency components were ignored and not considered in the insulator's frequency responses. The peak detection result did not have any considerable characteristics except for the peak at about 800 Hz. The entire average of the sound pressure level (SPL) on ambient noise was 30.51 dB and the average SPL from first to fifth harmonics of 120 Hz was 45.33 dB.

B. Noise Analysis

The comparison data for both the normal state and the fault state of the PI type 1 is shown in Fig. 8. Many spike signals and periodic components were found in the time signal of the fault state in Fig. 8(a). In the normal state, there are no significant components to be considered except some peaks at about 700 Hz, 12 kHz, and 17 kHz like the spectrum of the ambient noise in the anechoic. The fault state had a larger amplitude than

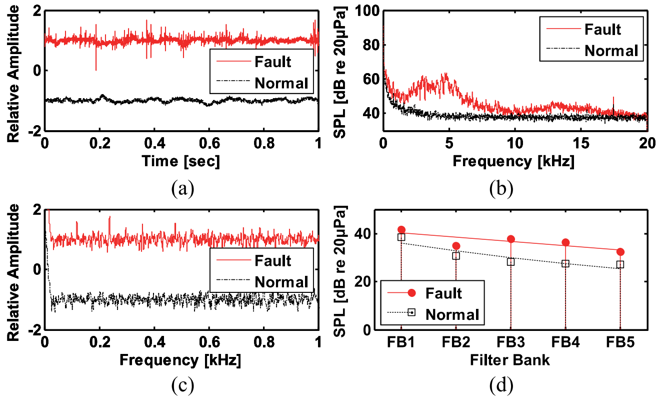

(a) (b) (c) (d)

Fig. 9. Comparison between the normal state and the fault state of the COS: (a) time signal, (b) frequency spectrum, (c) peak detection, and (d) filter bank and its fitting curve. The fault state had values 5.33 and 6.52 dB larger than those of the normal state in the entire average SPL and the average SPL from first to fifth harmonics of 120 Hz, respectively. The exponent values of normal and fault were − 0.09 and − 0.05, respectively.

the normal state through the entire spectrum, especially between 2 and 20 kHz, as shown in Fig. 8(b). There were outstanding harmonics of 120 Hz by the peak detection in a fault state, as shown in Fig. 8(c). The entire average SPL in both the normal state and the fault state were, respectively, 30.38 and 46.56 dB. The average SPL from first to fifth harmonics of 120 Hz in both the normal state and the fault state were 47.23 and 59.28 dB, respectively. The normal state had –0.13 and 1.90 dB larger values than the ambient noise in the entire average SPL and the average SPL from first to fifth harmonics of 120 Hz, respectively. The fault state had a value 16.18 dB larger on entire average SPL and a 8.13 dB larger on average SPL from first to fifth harmonics of 120 Hz than that of the normal state. In the result of the filter bank and its fitting curve in Fig. 8(d), the exponent part of the fault state has a larger value than the normal one.

Fig. 9 showed the measurement result of the COS. The entire characteristics of the wideband analysis and the harmonics of the 120 Hz looked like those of the PI type 1. The entire average SPL in the normal state was 30.52 dB and 35.86 dB in the fault state. The average SPL from first to fifth harmonics of 120 Hz in both the normal state and the fault state were 40.10 and 46.62 dB, respectively. The normal state had 0.02 and 0.19 dB larger values than the ambient noise in the entire average SPL and the average SPL from first to fifth harmonics of 120 Hz. The fault state had values 5.33 and 6.52 dB larger than that of the normal state in average of the entire spectrum and the harmonics, respectively.

Fig. 10 showed the measurement result of the LP type 1. The entire average SPL in both the normal state and the fault state were 30.31 and 38.06 dB, respectively. The average SPL from the first to fifth harmonics of 120 Hz in both the normal state and the fault state were 45.44 and 62.11 dB, respectively. The normal state had –0.19 and 0.12 dB larger values than the ambient noise in the entire average SPL and the average SPL from first to fifth harmonics of 120 Hz, respectively. The fault state had values 7.75 and 14.96 dB larger than that of the normal state in the entire average SPL and the average SPL from first to fifth harmonics of 120 Hz, respectively.

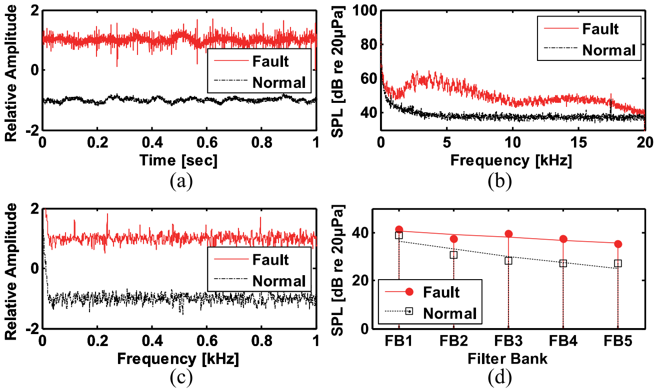

(a) (b) (c) (d)

Fig. 10. Comparison between the normal state and the fault state of the LP type 1 (L.P.1): (a) time signal, (b) frequency spectrum, (c) peak detection, and (d) filter bank and its fitting curve. The fault state had values 7.75 and 14.96 dB larger than those of the normal state in the entire average SPL and the average SPL from first to fifth harmonics of 120 Hz, respectively. The exponent values of normal and fault were − 0.09 and − 0.03, respectively.

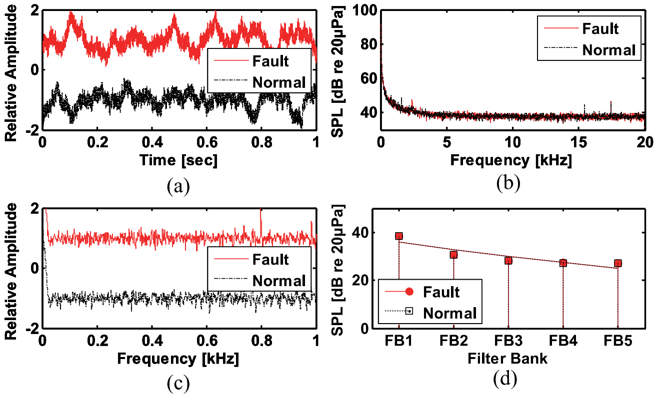

(a) (b) (c) (d)

Fig. 11. Comparison between the normal state and the fault state of the LA: (a) time signal, (b) frequency spectrum, (c) peak detection, and (d) filter bank and its fitting curve. The fault state had values 0.05 and – 0.28 dB larger than those of the normal state in in the entire average SPL and the average SPL from first to fifth harmonics of 120 Hz, respectively. Both exponent values of fault and normal were − 0.09.

Fig. 11 showed the measurement result of the lightning arrester. The characteristics were entirely different from the former three insulators. In the time signal, the difference between the fault state and the normal state was not found. In the wideband analysis and the harmonics of the 120 Hz, the insulator's spark also could not be determined. In addition, the frequency spectrums did not show any difference between each other, so it could not be detected by the difference in results of detection of a peak in a narrow band. The entire average SPL in the normal state was 30.55 dB, and 30.60 dB in the fault state. The average SPL from first to fifth harmonics of 120 Hz in both the normal state and the fault state were 45.37 and 45.31 dB, respectively. The normal state had 0.05 and 0.05 dB larger values than the ambient noise in the entire average SPL and the average SPL from first to fifth harmonics of 120 Hz. The fault state had values 0.05 and –0.28 dB larger than that of the normal state in

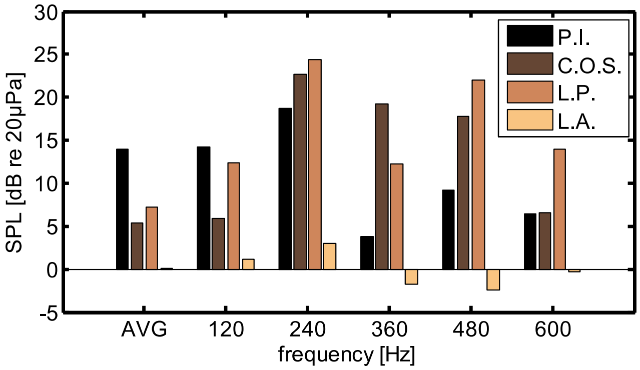

Fig. 12. Differences between the normal state and the fault state of the insulators. AVG means the mean total power in entire frequency response. Except LA, the SPL of the fault states are larger than those of the normal states.

TABLE IV
COMPARISON OF ALL RESULTS

Noise source (normal/fault)	Entire average SPL	Average SPL of harmonics of 120 Hz	Exponent value of fitting curve
Ambient noise	30.51	45.33	–0.09
PI	30.38	47.23	–0.09
	46.56	59.28	–0.03
COS	30.52	40.10	–0.09
	35.86	46.62	–0.05
LP	30.31	45.44	–0.09
	38.06	62.11	–0.03
LA	30.55	45.37	–0.09
	30.60	45.31	–0.09

All SPL's units are in dB.

the entire average SPL and the average SPL from first to fifth harmonics of 120 Hz, respectively. This meant that to figure out the fault state of the lightning arrester would be more difficult than other insulators. A possible way to determine the fault state of the lightning arrester would be diagnosis by thermal infrared camera, as shown in [2].

The difference between the normal state and the fault state of the insulators was shown in Fig. 12. AVG meant the entire average SPL of wideband analysis, and the other was the SPL of the harmonics of the 120 Hz in horizontal axis. In AVG, except for the lightning arrester, the fault state's values were larger than those of the normal state. The harmonics of the 120 Hz were also larger, except for the lightning arrester. From these two apparent results—the wideband analysis and the harmonics of the 120 Hz, the possibility of detecting the fault state of the insulators can be found, except for the lightning arrester. It can be concluded that the fault state's values are larger than the normal state's in both total average and 120 Hz harmonic components, as shown in Fig. 12. In the exponent value of curve fitting from result of filter bank, it was found that values of fault states were larger than normal state. For ease of comparison, results were summarized and shown in Table IV.

C. Noise Source Location

Per the previous section's result, the radiated noise had two significant features in the total average and 120 Hz harmonics components that could be detected by the microphone. The noise source location was evaluated by 3-D microphone array, as shown in Fig. 4. The source image plane's size is 3 m width and 3 m height. The number of the lattice points M × N were chosen as 200. So the size of image on source image plane has 15-mm (= 3 m/200 points) resolutions.

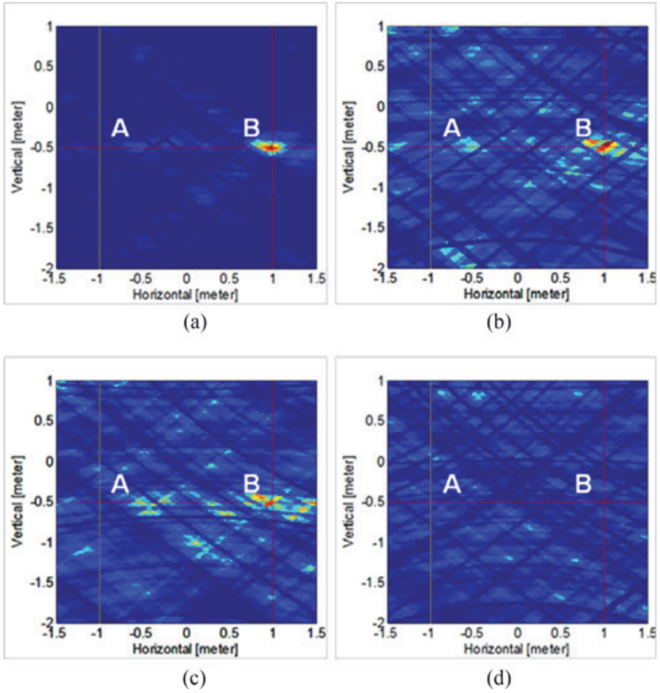

(a) (b) (c) (d)

Fig. 13. Source localization results: (a) PI, (b) COS, (c) LP, and (d) LA. The normal and fault state insulator are located in A and B, respectively. Three different type fault insulators were detected, except LA. The rectangular coordinates (*x*, *y*, *z*) m of A and B are (− 1.0, − 0.5, 3.0) m and (1.0, − 0.5, 3.0) m, respectively.

The insulator would be in a slightly lower position below the robot, so the reference sensor was chosen to be the nearest to it, as shown in Fig. 4. For the noise source location estimation with the 3-D microphone system, two insulators' locations were estimated at the same time. The normal and fault state insulators were located in A and B, respectively. The rectangular coordinates (x, y, z) m of A and B are (–1.0, –0.5, 3.0) m and (1.0, –0.5, 3.0) m, respectively. The results are shown in Fig. 13. The left cross line represents the position of a normal state insulator and the right cross line represents the position of a fault state insulator.

The entirety of the normal insulators was not detected. Meanwhile, the first three fault insulators were detected except for (d) lightening arrester (LA). Distance error is evaluated as the Euclidean norm between a source's coordinate B and the estimated coordinate, as shown in Table V. The first three insulators were very close to source B and the differences came from the value of the spectrum's average.

D. Fault Detection

The fault detection was evaluated using a NN. Per the results in Section IV-B, the combinations of total average and 120 Hz

TABLE V
FAULT LOCATION SOURCES ESTIMATION

Type	Auctual coordinate	Estimated coordinate	Distance error (m)
PI	(1.0, 0.5)	(0.975, 0.515)	0.03
COS	(1.0, 0.5)	(1.110, 0.530)	0.11
LP	(1.0, 0.5)	(1.125, 0.530)	0.12
LA	(1.0, 0.5)	NON	N/A

harmonic components were used for the input data. The datasets for the input layer were figured out and chosen by the following:

1) first data: the exponent part of the exponential curve fitting from the filter bank results;
2) second to sixth data: amplitudes of the harmonic component of 120 Hz;
3) seventh data: an average from 60 to 660 Hz.

For the NN, the numbers of layers were chosen as 7, 30, and 2 for the input, the hidden, and the output layer, respectively. These numbers were empirically chosen and then validated after variable numerical setting. The number of input layers depends on the frequency characteristics as given by the output of filter bank, peak signals, and average level. The number of output layers depends on the results from classification as given by normal or fault states.

The training data was the average of each insulator's one second length signal achieved from microphone channel 2. The data length was about 4 s in length, so that each average was obtained from four datasets. For the tolerance of the reference signal, the data was multiplied by 1.1 and divided by 1.1. Total training dataset resulted in six datasets from each insulator. The input data for the classification were 20 datasets, which consisted of four 1-s-length signals and a 4-s-length signal from two different microphone channels (achieved from channel 1 and channel 4).

The fault detection was evaluated from the four datasets using the confusion matrix in Fig. 14. It shows the performance of the classification algorithm with a table layout. It contains true positives (actually fault and classification output is also fault on first row/first column), false negatives (actually normal but classification output is fault on first row/second column), false positives (actually fault but classification output is normal on second row/first column), and true negatives (actually normal and classification output is also normal on second row/second column). There is one failure case regarding normal state as fault state on second row/first column in (a) PI and (b) COS So the total accuracy would be 95% (adding 10/10 in true positives and 9/10 in true negatives). The ratio 100% illustrates no error in classification. The highest detection ratio was 100% for (c) LP and others were relatively more than 95%, except (d) LA. The spectrum in LA was hard to distinguish between normal and fault state, thus, it reached 75% (adding 8/10 in true positives and 7/10 in true negatives).

The fault detection was also evaluated using other criteria calculated in Table V. The F_1 score, accuracy, and Matthews correlation coefficient (MCC) [26] were used for the four datasets. Table VI shows that these statistical values are consistently high among three metrics, especially the first three datasets. These statistical evaluations validated that the proposed acoustic fault detection system from insulators' radiation noises was feasible.

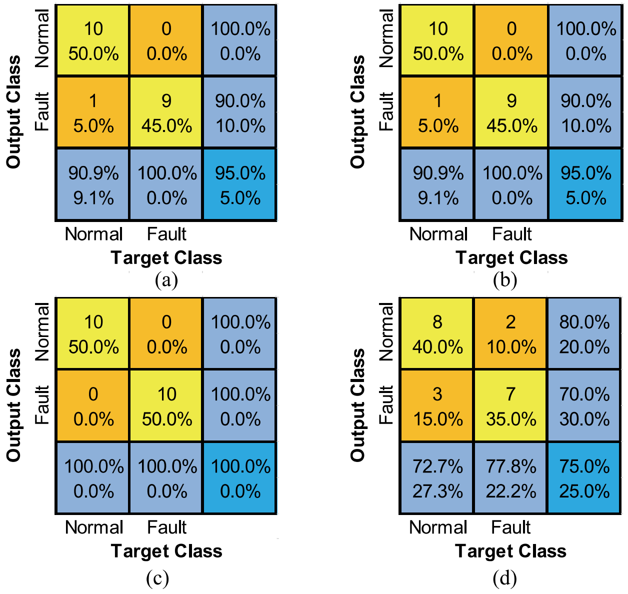

(a)

Output Class \ Target Class	Normal	Fault	
Normal	10 50.0%	0 0.0%	100.0% 0.0%
Fault	1 5.0%	9 45.0%	90.0% 10.0%
	90.9% 9.1%	100.0% 0.0%	95.0% 5.0%

(b)

Output Class \ Target Class	Normal	Fault	
Normal	10 50.0%	0 0.0%	100.0% 0.0%
Fault	1 5.0%	9 45.0%	90.0% 10.0%
	90.9% 9.1%	100.0% 0.0%	95.0% 5.0%

(c)

Output Class \ Target Class	Normal	Fault	
Normal	10 50.0%	0 0.0%	100.0% 0.0%
Fault	0 0.0%	10 50.0%	100.0% 0.0%
	100.0% 0.0%	100.0% 0.0%	100.0% 0.0%

(d)

Output Class \ Target Class	Normal	Fault	
Normal	8 40.0%	2 10.0%	80.0% 20.0%
Fault	3 15.0%	7 35.0%	70.0% 30.0%
	72.7% 27.3%	77.8% 22.2%	75.0% 25.0%

Fig. 14. The confusion matrix corresponding to Table II. (a) PI (b) COS (c) LP (d) LA.

TABLE VI
STATISTICAL EVALUATION

Type	F_1 score	Accuracy	MCC
PI	95.24	95.00	0.90
COS	95.24	95.00	0.90
LP	100.00	100.00	1.00
LA	76.19	75.00	0.50

The ratio 100% or 1.0 illustrate no error in classification.

To represent the effectiveness on our system with comparison with [2], there are differences in the following three areas. First, there were represented analysis results with wideband analysis, peak detection using sector space averaging technique, and exponent value from the curve fitting. Second, in source localization, comparing the results of [2] shown in Table V, it can be seen that there is almost no distance error. Also, the visual effect can be obtained by indicating on the source image plane where the noise is generated, as shown in Fig. 13. The noise source was detected with 100.0% accuracy for three typical conditions. Finally, from the analysis results, the fault detection was determined by NN to diagnose the state automatically. The highest detection ratio was 100% and others were relatively more than 95%, except LA.

V. CONCLUSION

In this paper, radiation noises were measured and analyzed from both the normal state insulators and the fault state insulators in the anechoic chamber. Two apparent results were found from their frequency spectrums—120 Hz harmonic components and higher average noise levels than normal state ones. The technique for the direction estimation of the fault state insulator using the cross correlation from the 3-D array microphones was also introduced. Finally, the classification technique using a NN was shown. It was also concluded that acoustic fault detection techniques are useful in the detection of insulator faults and the estimation of the direction of the fault state insulators. In addition, it was also demonstrated that the fault state of the lightning arrester is not distinguished from the normal state of that.

Future work includes larger scale datasets under the real outdoor environment with more radiation noise data and a high accuracy NN.

ACKNOWLEDGMENT

The authors would like to thank L. Linkous and A. Huynh for proofreading and helping to improve the paper.

REFERENCES

[1] W. R. Vincent, G. F. Munsch, R. W. Adler, and A. A. Parker, "The Mitigation of Radio Noise from External Sources at Radio Receiving Sites, 6th ed. Monterey, CA, USA: Naval Postgraduate School, 2007.

[2] H. Ha, S. Han, and J. Lee, "Fault detection on transmission lines using a microphone array and an infrared thermal imaging camera," IEEE Trans. Instrum. Meas., vol. 61, no. 1, pp. 267–275, Jan. 2012.

[3] K.-C. Park and J. R. Yoon, "Analysis of the insulators' radiation noises for error detections," in Proc. Symp. Ultrason. Electron., 2009, vol. 30, pp. 249–250.

[4] J. B. Dixit and A. Yadav, Electric Power Quality. New Delhi, India: Univ. Sci. Press, 2010, p. 2.

[5] IEEE Recommended Practice for Monitoring Electric Power Quality, IEEE Standard 1159-2009, 2009.

[6] A. Vidal et al., "Assessment and optimization of the transient response of proportional-resonant current controllers for distributed power generation systems," IEEE Trans. Ind. Electron., vol. 60, no. 4, pp. 1367–1383, Apr. 2013.

[7] M. Savaghebi, A. Jalilian, J. C. Vasquez, and J. M. Guerrero, "Autonomous voltage unbalance compensation in an islanded droop-controlled microgrid," IEEE Trans. Ind. Electron., vol. 60, no. 4, pp. 1390–1402, Apr. 2013.

[8] M. Valtierra-Rodriguez, R. De Jesus Romero-Troncoso, R. A. Osornio-Rios, and A. Garcia-Perez, "Detection and classification of single and combined power quality disturbances using neural networks," IEEE Trans. Ind. Electron., vol. 60, no. 5, pp. 2473–2482, May 2014.

[9] D. Chen, J. Zhang, and Z. Qian, "An improved repetitive control scheme for grid-connected inverter with frequency-adaptive capability," IEEE Trans. Ind. Electron., vol. 60, no. 2, pp. 814–823, Feb. 2013.

[10] Y. F. Wang and Y. W. Li, "Three-phase cascaded delayed signal cancellation PLL for fast selective harmonic detection," IEEE Trans. Ind. Electron., vol. 60, no. 4, pp. 1452–1463, Apr. 2013.

[11] J. Wang, Q. He, and F. Kong, "Adaptive multiscale noise tuning stochastic resonance for health diagnosis of rolling element bearings," IEEE Trans. Instrum. Meas., vol. 64, no. 2, pp. 564–577, Feb. 2015.

[12] S. Choi, B. Akin, M. M. Rahimian, and H. A. Toliyat, "Performance-oriented electric motors diagnostics in modern energy conversion systems," IEEE Trans. Ind. Electron., vol. 59, no. 2, pp. 1266–1277, Feb. 2012.

[13] B. Akin, S. Choi, U. Orguner, and H. A. Toliyat, "A simple real-time fault signature monitoring tool for motor-drive-embedded fault diagnosis systems," IEEE Trans. Ind. Electron., vol. 58, no. 5, pp. 1990–2001, May 2011.

[14] J. Kim and B. You, "Fault detection in a microphone array by intercorrelation of features in voice activity detection," IEEE Trans. Ind. Electron., vol. 58, no. 6, pp. 2568–2571, Jun. 2011.

[15] S. A. Zekavat and R. M. Buehrer, Handbook of Position Location: Theory, Practice and Advances, 1st ed. Hoboken, NJ, USA: Wiley, 2011.

[16] R. A. Mucci, "A comparison of efficient beamforming algorithms," IEEE Trans. Acoust., Speech, Signal Process., vol. ASSP-32, no. 3, pp. 548–558, Jun. 1984.

[17] B. Friedlander, "A sensitivity analysis of the MUSIC algorithm," IEEE Trans. Acoust., Speech, Signal Process., vol. 38, no. 10, pp. 1740–1751, Oct. 1990.

[18] J.-R. Yoon and S. A. L. Glegg, "Microphone array design for noise source imaging," Korean Soc. Noise Vib. Eng., vol. 7, no. 2, pp. 255–260, 1997, [in Korean].

[19] I. Jouny, F. D. Garber, and R. L. Moses, "Radar target identification using the bispectrum: A comparative study," IEEE Trans. Aerosp. Electron. Syst., vol. 31, no. 1, pp. 69–77, Jan. 1995.

[20] G. Moschioni, B. Saggin, and M. Tarabini, "3-D sound intensity measurements: Accuracy enhancements with virtual-instrument- based technology," IEEE Trans. Instrum. Meas., vol. 57, no. 9, pp. 1820–1829, Sep. 2008.

[21] J. D. Maynard, E. G. Williams, and Y. Lee, "Nearfield acoustic holography: I. Theory of generalized holography and the development of NAH," J. Acoust. Soc. Amer., vol. 78, pp. 1395–1413, 1985.

[22] G. C. Carter, A. H. Nuttall, and P. Cable, "The smoothed coherence transform," Proc. IEEE, vol. 61, no. 10, pp. 1497–1498, Oct. 1973.

[23] M. P. Oliveri, "A broadband signal processor for acoustic imaging using ambient noise," M.S. thesis, Dept. Ocean Eng., Florida Atlantic Univ., Boca Raton, FL, USA, 1994.

[24] R. O. Nielsen, Sonar Signal Processing. Norwood, MA, USA: Artech House, 1991.

[25] Neural Network Toolbox. [Online]. Available: https://www.mathworks.com/help/nnet/index.html

[26] D. M. W. Powers, "Evaluation: From precision, recall and F-measure to ROC, informedness, markedness & correlation," J. Mach. Learn. Technol., vol. 2, pp. 37–63, 2011.

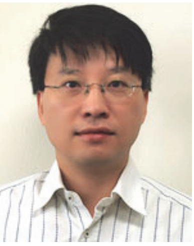

Kyu-Chil Park received the B.S. and M.S. degrees from the Department of Electronic Engineering, Pukyong National University, Busan, South Korea, in 1993 and 1995, respectively, and the Ph.D. degree from the Graduate School of Natural Science and Technology, Okayama University, Okayama, Japan, in 2000.

Since 2002, he has been a Professor in the Department of Information and Communications Engineering, Pukyong National University. His research interests include underwater acoustic signal processing, adaptive signal processing, numerical analysis, optimization, and inverse problems in engineering.

Yuichi Motai (S'00–M'03–SM'12) received the B.Eng. degree in instrumentation engineering from Keio University, Tokyo, Japan, in 1991, the M.Eng. degree in applied systems science from Kyoto University, Kyoto, Japan, in 1993, and the Ph.D. degree in electrical and computer engineering from Purdue University, West Lafayette, IN, USA, in 2002.

He is currently an Associate Professor of electrical and computer engineering at Virginia Commonwealth University, Richmond, VA, USA. His research interests include the broad area of sensory intelligence, particularly in medical imaging, pattern recognition, computer vision, and sensory-based robotics.

Jong Rak Yoon received the M.S. and Ph.D. degrees in ocean engineering from Florida Atlantic University, Boca Raton, FL, USA, in 1987 and 1990, respectively.

From 1979 to 1985, he was a Research Scientist with the Agency for Defense Development. Since 1990, he has been a Faculty Member in the Department of Information and Communications Engineering, Pukyong National University, Busan, South Korea. His research interests include underwater acoustics and underwater acoustic signal processing with an emphasis on underwater acoustic signal measurement/analysis, classification, and underwater acoustic communication.

Dr. Yoon is a member of the Acoustical Society of America.